Microimaging VIS-IR spectroscopy of ancient volcanic rocks as Mars analogues

Paola Manzari, Simone de Angelis, Maria Cristina de Sanctis, Tatiana Di Iorio, Eleonora Ammannito, Nicolas Bost, Frédéric Foucher, Frances Westall

AGU PUBLICATIONS

Earth and Space Science

RESEARCH ARTICLE
10.1002/2015EA000153

Key Points:
- Comparison between punctual and imaging spectrometers on Mars analogues
- Mineralogy of basic and acidic volcanic rocks through spectral imaging
- Very good agreement of the results obtained with different techniques

Correspondence to:
P. Manzari
paola.manzari@iaps.inaf.it

Citation:
Manzari, P., S. De Angelis, M. C. De Sanctis, T. Di Iorio, E. Ammannito, N. Bost, F. Foucher, and F. Westall (2016), Microimaging VIS-IR spectroscopy of ancient volcanic rocks as Mars analogues, *Earth and Space Science*, *3*, 268–281, doi:10.1002/2015EA000153.

Received 21 DEC 2015
Accepted 1 APR 2016
Accepted article online 11 APR 2016
Published online 14 JUL 2016

Microimaging VIS-IR spectroscopy of ancient volcanic rocks as Mars analogues

Paola Manzari[1], Simone De Angelis[1], Maria Cristina De Sanctis[1], Tatiana Di Iorio[2], Eleonora Ammannito[3], Nicolas Bost[4], Frédéric Foucher[5], and Frances Westall[5]

[1]INAF-IAPS—Institute for Space Astrophysics and Planetology, Rome, Italy, [2]ENEA, UTME-TER, Roma, Italy, [3]Department of Earth, Planetary and Space Sciences, University of California, Los Angeles, California, USA, [4]CNRS, CEMHTI UPR 3079, Université d'Orléans, Orléans, France, [5]Centre de Biophysique Moleculaire, UPR CNRS4301, Orléans, France

Abstract The SPectral Imager (SPIM) facility is a laboratory VIS-IR spectrometer developed to support spaceborne observations of rocky bodies of the solar system. Currently, this laboratory setup is used to support the Dawn NASA mission and to support the 2018 ExoMars mission in the spectral investigation of Martian subsurface. Specifically, for this mission, a selection of relevant Mars analogue materials has been characterized and stored in the International Space Analogue Rockstore (ISAR), hosted in Orléans, France. In this investigation, two volcanic rock samples from the ISAR collection were analyzed. These two samples were chosen because of their similarity in mineralogical composition and age with Martian basalts and volcanic sands. Moreover, volcanic sands are particularly interesting because they can contain fossils of primitive life forms. The analysis of data collected by SPIM resulted in good agreement with the mineralogical phases detected in these two samples by mineralogical and petrographical techniques, demonstrating the effectiveness of the high spatial and spectral resolution of SPIM for identifying and for mapping different mineralogical species on cut rock and mineral samples.

1. Introduction

The future 2018 mission of the ExoMars program will deliver a European rover and a Russian surface platform to the surface of Mars [*Vago et al.*, 2013].

Since one of the objectives of the mission is the identification of geological materials that could potentially preserve ancient traces of life [*Vago et al.*, 2013], the ExoMars rover will use a suite of complementary instrumentation including a drill, thus allowing core sampling down to a depth of 2 m. The panoramic camera PanCam and the close-up imager CLUPI will be used to obtain context, structural, and textural information from the kilometer to the millimeter scale. The ISEM (pencil-beam IR spectrometer) will be used to determine the target soil/rock bulk mineralogical composition at distance. The mineralogy of the borehole is determined by the visible-IR spectrometer "Mars Multispectral Imager for Subsurface Studies" (Ma_MISS) [*Coradini et al.*, 2001]. In the analytical laboratory, the mineralogy will be determined by the infrared spectrometer MicrOmega and the Raman Laser Spectrometer.

In order to constitute a reference library for spectroscopic identification of materials, *Bost et al.* [2013] developed a collection named the International Space Analogue Rockstore (ISAR) in Orléans, France. In this collection, minerals and rocks were characterized by mineralogical and petrographical techniques, with the aim of supporting diffuse reflectance spectroscopy in the visible and near-infrared range.

Furthermore, as it is an experiment to test identification of unknown samples using ExoMars instrumentation, the ISAR group solicited instrument teams to participate in a blind test on two selected rocks from the ISAR collection. The unknown samples were investigated by Ma-Miss [*De Angelis et al.*, 2014], MicrOmega, and Raman Laser Spectrometer. The results, supplemented by satellite images and photographs of the outcrops, comparable to satellite images and PanCam photographs on Mars, were then compiled and submitted to a team of geologists for blind interpretation.

Here the two ISAR samples belonging to the "blind test" experiment [*Bost et al.*, 2015] were analyzed by means of both a Fieldspec spectrometer and the SPectral Imager (SPIM) for testing the SPIM ability to identify mineral end-members in rock slabs and mixtures. The SPIM is a visible and infrared imaging spectrometer that is a spare of the one on board the Dawn spacecraft [*De Sanctis et al.*, 2010; *Coradini et al.*, 2011].

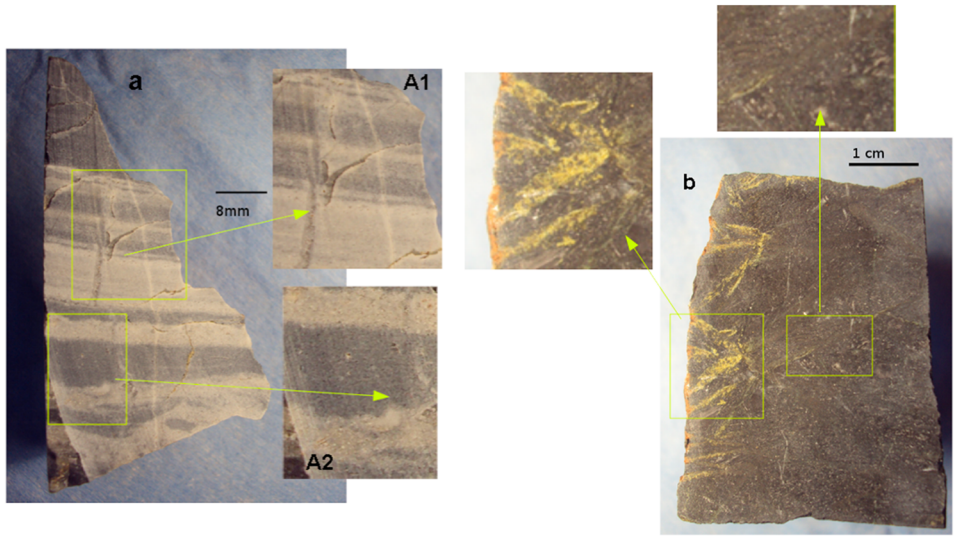

Figure 1. (a) Sample A and the two regions investigated by SPIM named A1 e A2; (b) Sample B and the two regions investigated by SPIM.

2. Petrography of Samples

The terrestrial samples selected by ISAR were chosen on the basis of their compositional similarity with Martian rocks and with respect to the preservation of organic traces of fossil microbial life. This information, originally, was all that was known about the samples. All the rocks from this collection had been previously fully characterized using X-ray diffraction (XRD), Raman spectroscopy, IR spectroscopy, optical microscopy, Scanning Electron Microscopy (SEM), and Electron Microprobe (EMP) in the framework of the ISAR project [*Bost et al*., 2013; 2011]. From this collection, two samples labeled "sample A" and "sample B" were chosen for the blind test.

2.1. Sample A

Named 00 AU05 in the ISAR collection, sample A (Figure 1a) had a fine-grained appearance and was characterized by light- and dark-colored layers. Visual observation and thin section analysis showed that the differences in color between the black and white layers are related to grain size, the darker layers being finer grained than the white ones [*Bost et al*., 2015]. The outcrop from which the sample originated, 3.446 Gy-old Kitty's Gap Chert of the Panorama Formation in the Warrawoona Group of the Pilbara Craton, Australia [*de Vries*, 2004; *Westall et al*., 2006], consists of laminated black and white chert representing silicified volcanic sands and silts deposited in a mud flat/tidal channel environment [*de Vries et al*., 2006]. Sedimentary structures, including ripple, channel, and flaser bedding, are clearly visible at the outcrop scale and also in hand specimen. The sediment contains cryptic morphological and carbonaceous traces of life [*Westall et al*., 2006, 2011; *Orberger et al*., 2006]. The ISAR sample is characterized by submillimeter- to millimeter-thick black and white laminae. The major components of sample KG 1 (Kitty's Gap1) are microcrystalline quartz (85–90 vol %) and hydromuscovite. The white and black laminae show different textures and grain size related to local variations in the depositional environment, the white layers consist of coarser-grained volcanic clasts than the black layers. Thus, there is no difference in the mineralogy between the black and white layers. The black laminae are fine grained and contain fewer porphyroclasts, which are now ghost clasts (i.e., replaced by silica), than the white laminae. Three types of ghost clasts have been distinguished: (1) euhedral to subhedral crystal shapes, replaced by hydromuscovite and outlined by nanometer-sized Ti-oxide spherules; (2) euhedral crystals (100–300 μm) replaced by hydromuscovite; and (3) euhedral ghost crystals with aggregates of hydromuscovite and Ti-oxides intergrown with quartz. Precursors of these crystals are interpreted to be either Ti-bearing mica, K-feldspar, or amphibole. Anhedral aggregates of hydromuscovite and minor quartz, outlined by Ti-oxide spherules, could represent glass shards or mineral debris [*Orberger et al*., 2006]. Organic matter occurs as clusters around the volcanic clasts or as delicate mats on laminae surfaces and also as detrital particles [*Westall et al*., 2006].

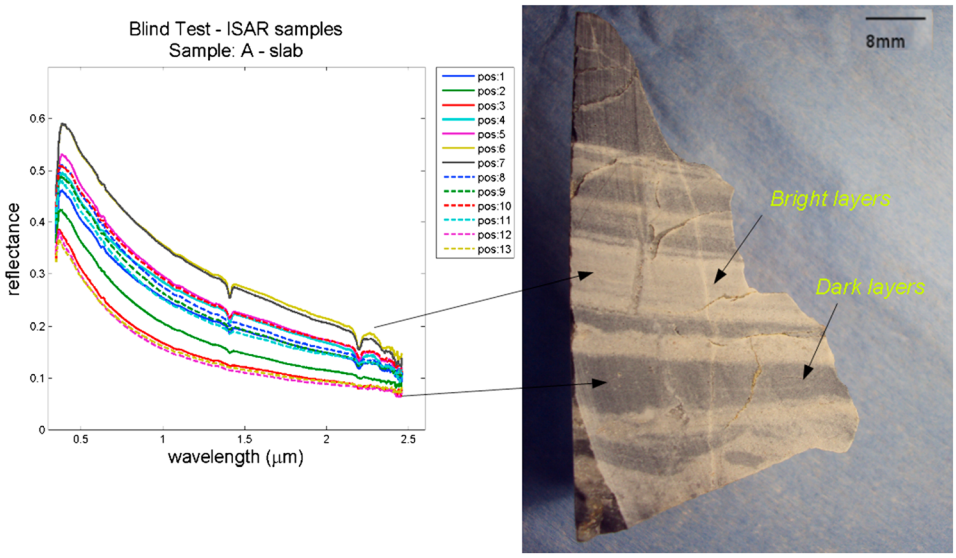

Figure 2. Fieldspec spectra of sample A (slab). The spectra were acquired on 13 positions along the slab. They all show similar features, characterized by a negative blue slope toward the NIR, with no absorption bands other than the one at 1.4 μm (OH) and the one at 2.2 μm (Al-OH). The different levels of albedo of the spectra are indicative of the alternating dark and bright layers of this sample.

2.2. Sample B

Named 10ZA09 in the ISAR collection, this sample (Figure 1b) is an altered, silicified komatiite basalt displaying spinifex texture, originating from the type locality on the Komatii River in the Barberton Greenstone Belt, South Africa. The sample comes from the Kromberg formation (3.42–3.33 Gy) in the Onverwacht group. Although these rocks have been affected by lower greenschist regional metamorphism, the structure and the bulk chemical composition, however are, still preserved. Silicification aided preservation of the rock although it also induced a marked loss of the labile elements Ca, Al, and Mg. The weathered surface of the rock shows altered spinifex texture, while the cut surface is textureless and has an almost glassy appearance. Thin section study documents significant alteration. Although the sample still exhibits the typical olivine spinifex texture, the olivines are totally altered to amphibole and phyllosilicates. Some talc fibers can be observed. The other major phases, such as pyroxenes, are also altered to talc, micas, and phyllosilicates (originally clays, now mica). Some accessory grains of iron oxide, such as hematite, occur together with dolomite [*Bost*, 2012]. The komatiite samples are particularly relevant because they are primitive Mg-rich basic volcanics, typically abundant in the Archean period on Earth and possibly on Mars in Noachian terrains [*Nna-Mvondo and Martinez-Frias*, 2007; *Mangold et al.*, 2009; *Bost et al.*, 2012].

3. Experimental Setups

Each of the two samples was analyzed both in the form of slab and powder by means of FieldSpec spectrophotometer and by the spectral imager SPIM.

The Fieldspec spectrophotometer operates in the range between 0.35 and 2.50 μm. The Fieldspec, mounted on a goniometer, acquired spectra in standard conditions with an illumination angle $i = 30°$ and an emission angle $e = 0°$. The size of illuminated spots, on the target, has a diameter of 6 mm.

The spectrometer consists of three detectors, the first between 0.35 μm and 1 μm, the second between 1 μm and 1.8 μm, and the third up to 2.5 μm. The spectral resolution is 3 nm for the first detector and 10 nm for the others; the spectral sampling is respectively 1.4 nm and 2 nm.

The SPectral IMaging (SPIM) facility is a laboratory setup that has been developed to support remote sensing observations of solar system bodies [*Coradini et al.*, 2011; *De Angelis et al.*, 2015]. It operates in a wide spectral range, 0.3–5.1 μm and is characterized by high spatial (38 μm) and spectral (2 nm in the VIS channel, 12 nm in the IR channel) resolution. The spectral coverage is obtained by two bidimensional focal plane arrays, one for the visible between 0.25 and 1.05 μm with a spectral resolution of 2 nm and one for the IR between 0.95 and

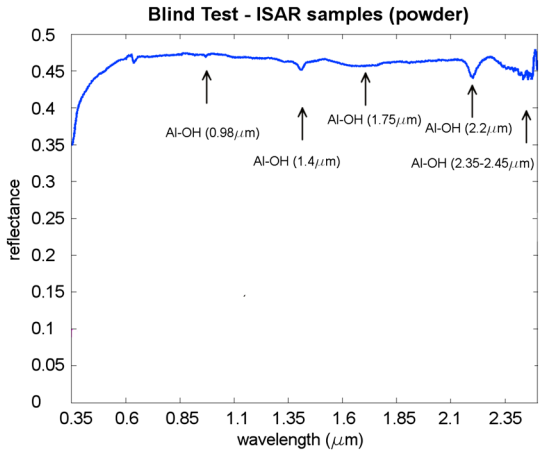

Figure 3. Fieldspec spectrum of powdered sample A.

5.05 μm with a spectral resolution of 12 nm. The bidimensional focal planes aligned with the spectrometer's 9 mm slit axis permit the acquisition of the target's image of 0.038 × 9 mm at different wavelengths [*De Angelis et al.*, 2015]. The sample scan takes place by acquiring *N* spectra along the slit and then moving the slit. The spectra on the slab are not averaged, whereas 1000 of the spectra are averaged on powders. The reflectance calibration is obtained acquiring Spectralon Labsphere reflectance standards with reflectance values similar to the analyzed rocks (5–40%).

For each spectrum the background measurement is performed by acquiring signal without illuminating the target, and it is subtracted from the measurement on the illuminated sample and the standard reference used. The construction of the hyperspectral cube takes place by acquiring the spectra along a line of pixels (the slit: 9 × 0.038 mm) on the sample, and then moving the sample one step equal to the width of the slit itself (0.038 mm). By acquiring *N* successive lines (one spectrum for each pixel), a hyperspectral cube is built. For what concerns about the studies on single absorption feature, the continuum to be removed consisted of first-order polynomial passing between two points at fixed wavelengths. Instead, for the whole spectrum, the continuum consisted of a second-order polynomial fitting the entire spectrum. The identification of spectra was performed by means of Reflectance Experiment Laboratory (RELAB) and United States Geological Survey (USGS) spectral databases.

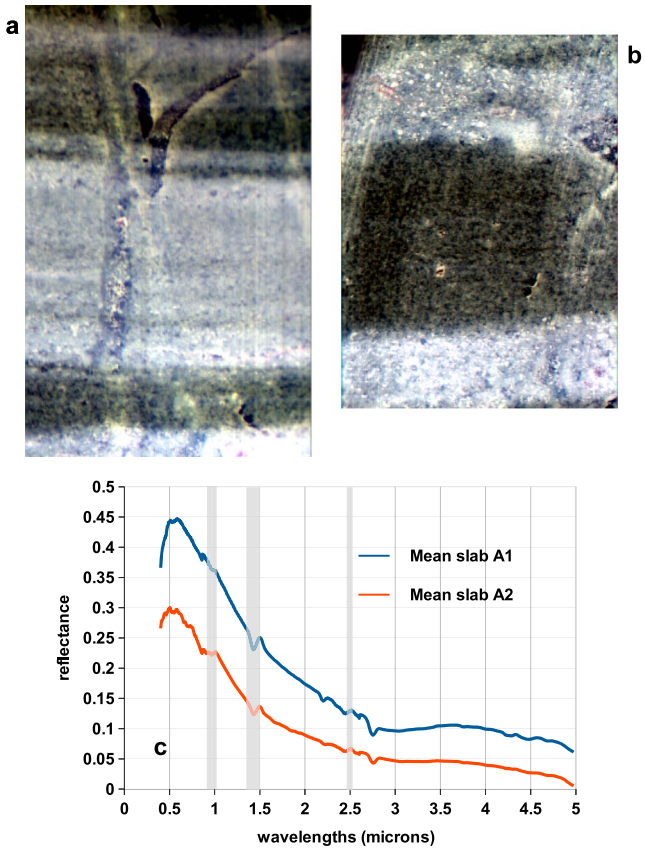

Figure 4. RGB (450; 560; 680 nm) image of the regions (a) A1 and (b) A2 of the sample A. (c) Average spectra related to A1 and A2 areas. Shaded areas are placed where bands should be excluded from the interpretation because of filters and VIS-IR junction.

4. Results

4.1. Sample A—Fieldspec

Fieldspec data were collected both on slab and on powder. The reflectance value never exceeded 0.7 in the bright layers, whereas it remains under 0.3 in the dark layers. Data on the slab were acquired at 13 different positions generally corresponding to bright and dark layers (Figure 2). The spectra on the slab are generally characterized by a steep negative slope in the VNIR and two absorption features at 1.4 μm and 2.2 μm that correspond to O-H and Al-OH bonds, respectively. The spectrum of powders shows other absorption features at λ = 0.98; 1.75; 2.35–2.45 μm that are related to Al-OH bonds (Figure 3).

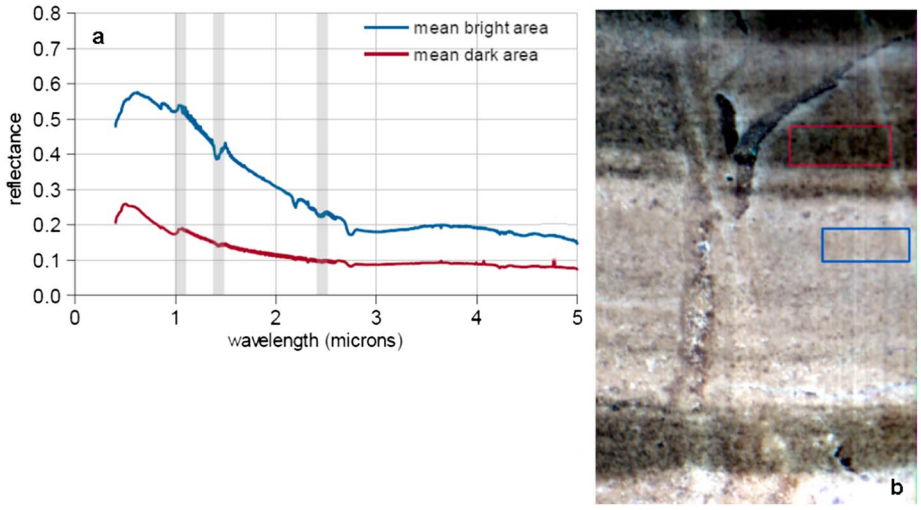

Figure 5. (a) Average profiles of bright and dark areas, corresponding to the area selected in Figure 5b. The number of pixels in the selected areas are the same.

4.2. Sample A—SPIM

By means of SPIM, data were acquired on two selected areas on the slab (Figures 4a and 4b) named A1 and A2. The spectral profiles are dominated by negative slope and few absorption bands. Area A2 with respect to A1 seems to be more affected by deeper absorptions in the visible range, around 0.8–0.9 μm (Figure 4c). In Figure 5 the mean spectra of bright and dark layers of A1 are shown. These spectra show a negative slope that is more evident in the bright areas (Figure 5a). This negative slope continuum affects absorption feature position, shifting band centers slightly toward greater wavelengths. Moreover, the two areas show slightly different spectral profiles.

The negative slope typical of all pixel spectra matches that of chert (Figure 6a) and, in general, of micro/cryptocrystalline siliceous rocks.

Furthermore, several absorption features are superimposed on this negative slope profile spectrum. As can be seen in Figure 6a, superposition of different absorptions probably related to different minerals on the spectrum is visible also on the spectrum related to only one pixel. In fact, although spectra show generally a negative slope, regardless of dark or bright layer area, they were characterized by several different little absorption features.

Since SPIM has filter junctions at 1.4 and 2.5 μm, the absorptions in these bands must be excluded from the interpretation of SPIM spectra. Therefore, the approach followed to optimize the SPIM data analyses was to examine, first, sample data from the bright layers, in which 1.4 and 2.5 μm absorptions were more evident by

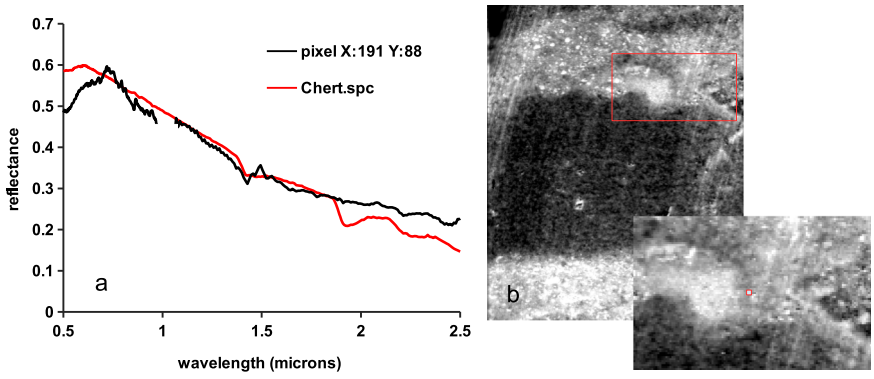

Figure 6. Spectral comparison between chert and the spectral profile of (a) pixel x191y88; (b) pixel x191y88 corresponds to the red dot on the right image of area A2; pixel size is 38 × 38μm.

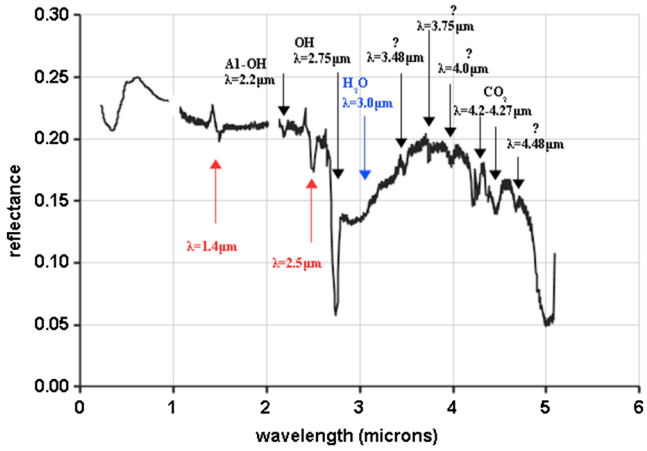

Figure 7. Average spectral profile of powders as collected by SPIM.

means of Fieldspec and then in the dark ones. In this way we focus the attention, first, on identifying phyllosilicates end-members. We then proceeded to investigate different Al-phyllosilicates, since pixel spectra showed strong Al-OH absorption at 2.2 μm (Figure 7).

Finally, we proceeded to analyze those pixels where Al-OH absorptions were absent or weak for identifying other phases. Dark layers were characterized by strong absorptions in the 0.8–0.9 μm range.

4.2.1. Mineral Components in Samples A1 and A2

The identification of the mixture was made by removing the continuum and comparing each absorption band with library data. The continuum was a linear function for a single absorption feature, and n-polynomial function for wider ranges.

4.2.1.1. Muscovite/Illite

The identification was made after having previously selected all the pixels with a spectral feature at about 2.2 μm, so as to find the pixel with the most evident 2.2 spectral feature. On these pixels, the copresence of absorption at around 2.2 μm and 2.35 μm confirmed the occurrence of K-Al-phyllosilicates as muscovite or illite (Figure 8a). Note that the 2.45 μm band could not be taken into account because of the presence of the filter.

Mapping of the 2.2 μm band depth (Figure 9) was made in order to find the spatial distribution of stronger depths (values between 0.2 and −0.05). In addition, mapping of the band center in the range 2.18–2.22 mm was calculated for comparison with band depth map. In Figure 9, the depth between −0.1 and −0.008 of the 2.2 absorption was mapped both on slab A1 and slab A2.

4.2.1.2. Rutile/Anatase

The strong absorption between 0.4 and 0.6 in some pixels, for example, pixel x107y136 or x92y200 (Figures 10 and 11), could be related to the occurrence of TiO_2. The Modified Gaussian Model (MGM) [*Sunshine et al.*, 1990] was computed first in the range of 0.4 and 0.7 μm to extract depth and band center of pixel 92–200 (Figure 10a) by means of an Interactive Data Language algorithm. The resulting band center was 0.55 μm whereas the band depth was −0.17. Finally, both band center and depth were calculated for each pixel of the image and then superimposed onto the band image to map only the deepest absorption pixels in the range between 0.4 and 0.7 μm. The deepest absorption features, with band center between 0.45 and 0.6 μm are depicted in red in Figure 11b (red spots on slab A1) that correspond to spectra on Figure 11a. Figure 11 shows the occurrence of a strong wide absorption between 0.5 and 0.6 μm that matches the spectral feature of rutile.

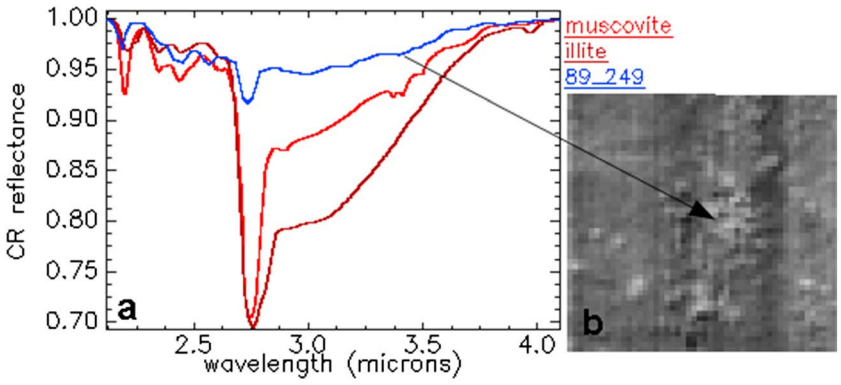

Figure 8. (a) Continuum removed spectral comparison between muscovite, illite, and pixel x89y249 of area A1 figure. (b) Pixel size is 38 × 38 ⊠m.

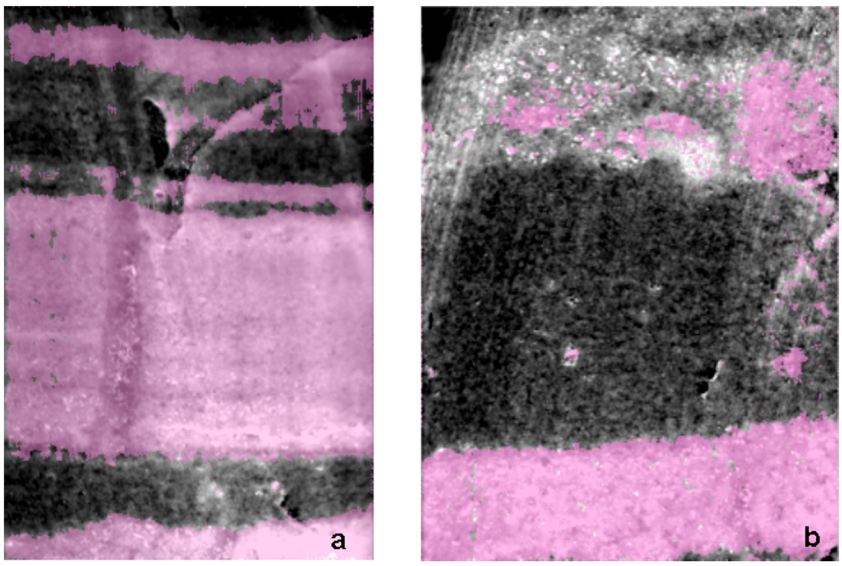

Figure 9. Mapping of the deepest 2.2 μm band (purple-shaded areas) on (a) A1 and (b) A2.

4.2.1.3. Goethite

Two absorptions around 0.65 and 0.95 μm could be related to goethite occurrence (Figure 12a). The calculated parameters of the interpreted goethite in pixel x123y145 are band center 0.94 μm, depth value –0.12 (Figure 12c).

Finally, different features in the 3.2 to 3.5 μm range were found especially in the dark region of sample A, in particular, around 3.22–3.25 and 3.4 μm (Figure 13). Absorption features related to both C-H and C-O bonds occur in this spectral region. Thus, the features found in the spectra of the pixels documented in Figure 13 were inferred to be related to carbonaceous matter and kerogen; absorptions around 2.75 μm are related to the OH bond, whereas 3.3, 3.9, and 4.6 μm could be related to organic compounds or carbonates [*Gaffey*, 1985, 1986] and those near 3.25, 3.4, 3.75, and 4.5 μm to C-O and C-H bonds.

4.3. Sample B—Fieldspec

This sample was subdivided into two analyzed regions labeled "dark" and "bright." In the bright region antigorite and glass were detected by means of the Fieldspec spectrometer. Antigorite/serpentine group spectra were obtained from the bright/yellowish regions, whereas basaltic glass-like spectra occurred in the black ones (Figure 14).

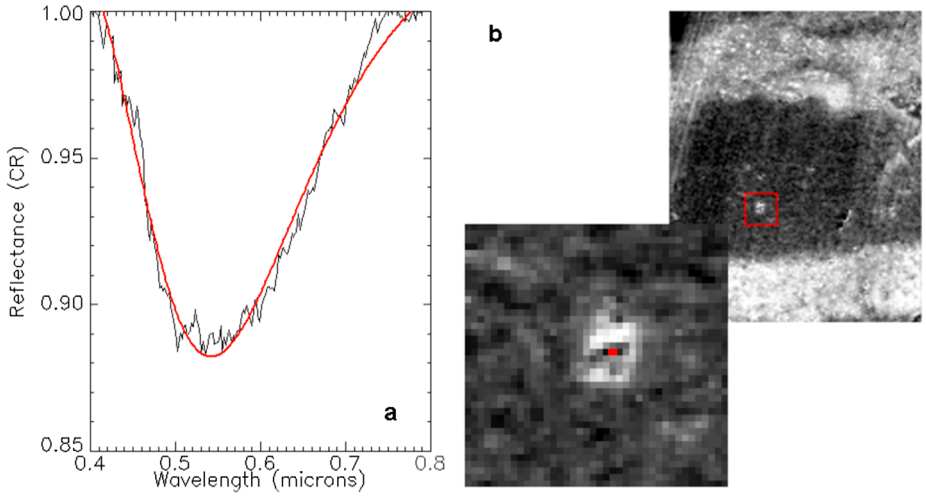

Figure 10. Spectral band (with the continuum removed) corresponding to (a) pixel x92y200; (b) pixel x92y200 in A2.

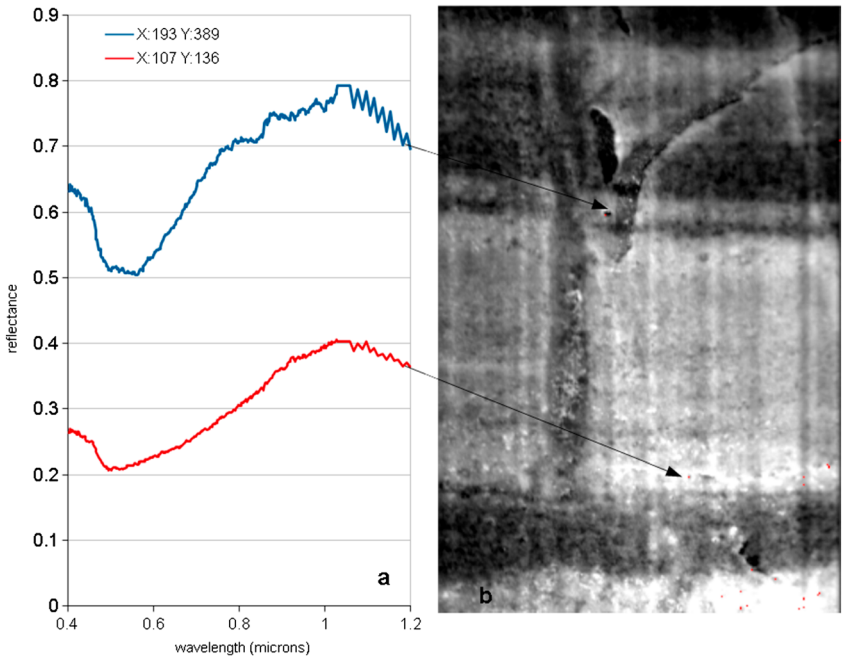

Figure 11. (a) TiO_2 spectral profiles corresponding to (b) the two pixels.

4.4. Sample B—SPIM

As for sample A, also on sample B two areas were investigated: "bright" and "dark" (Figures 15a and 15b). Unsupervised classification algorithms are used in remote sensing for clustering pixels that result spectrally similar. These algorithms applied on hyperspectral images produce spectral maps. In this study, isodata

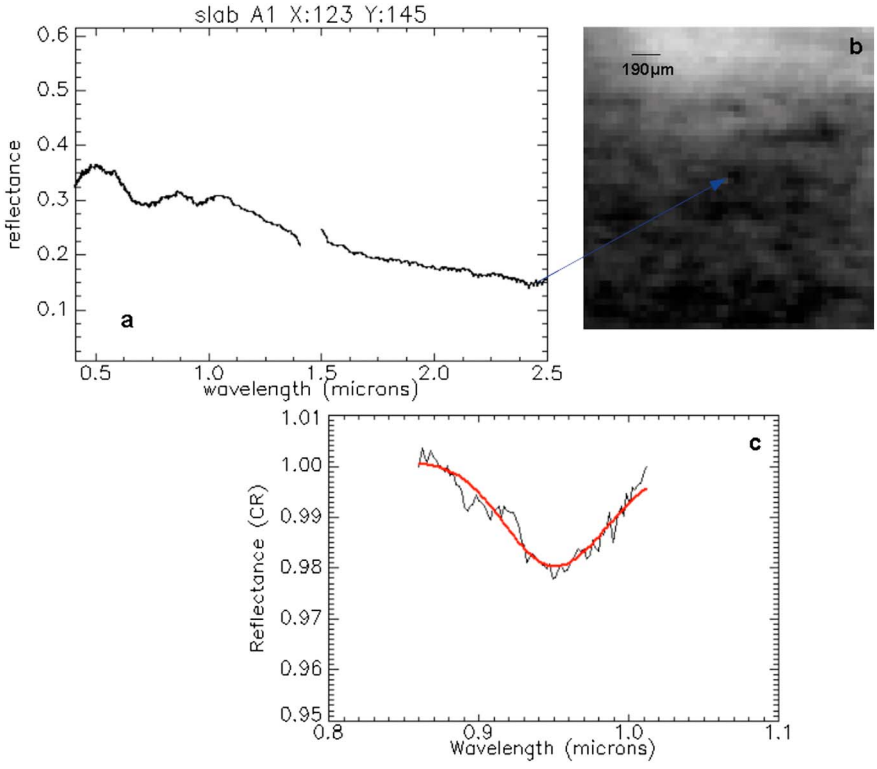

Figure 12. Spectral profile of (a) pixel x123y145; (b) pixel x123y145; pixel's dimensions are 38 × 38 µm; (c) continuum removed band and Gaussian fit for extracting band minimum and depth.

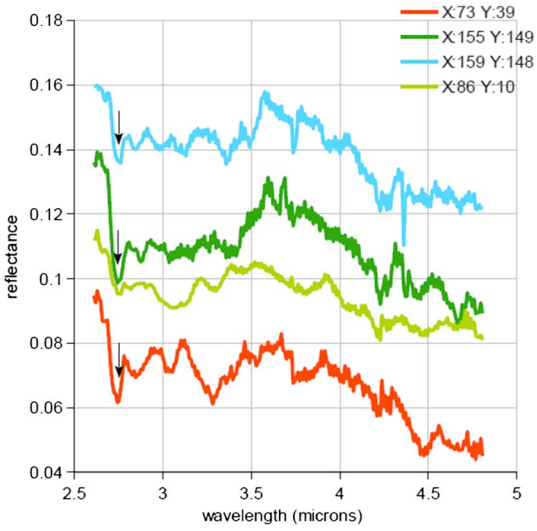

Figure 13. Spectral profiles related to those pixels in dark layers characterized by absorptions in the range between 2.6 and 4.6 μm.

algorithm was computed using the SPIM data from the two areas, dark and bright, of this sample in order to compare the spectral similarity. Identification of mineralogical phases was first done on those pixels belonging to classes found by isodata algorithm (Figure 15c).

In this way, it was possible to confirm the serpentine group composition of the "yellowish" areas of the bright fragment. These areas are yellow and brown colored on the isodata image. The dark regions show a blue negative slope that is typical of fine-grained rock slabs. The spectral profiles related to the classes found by isodata show absorption features belonging to mixed minerals, as shown from the comparison with RELAB and USGS spectral libraries. Some phyllosilicates and amphiboles were identified on the basis of absorption features near 2.75 μm, also taking into account that part of this feature could be probably due to adsorbed water.

4.4.1. Mineral Components in Sample B

Several phases were found in sample B. The serpentine group minerals was found to match some classes of spectra (Figure 16a). In particular, in Figure 17, pixel profiles classified as antigorite are compared with antigorite from spectral libraries in two different ranges: 0.4–3 μm (Figure 17a) and 1.5–5 μm (Figure 17b). As it can be seen, phlogopite, antigorite, and talc (Figures 17–19) were identified mainly by removing the continuum in the range between 2.1 and 4.1 μm to study the 2.75 μm absorption and then checking again their other characteristic absorptions in the VNIR range, (see talc, Figure 19a).

5. Discussion

5.1. Interpretation of the Results: Negative Slope of Slab Samples A and B

Samples A and B are both fine-grained rocks. In both a difference between slab and powders is observed from a spectroscopic point of view. In fact, the spectra of the slabs of the two samples are characterized

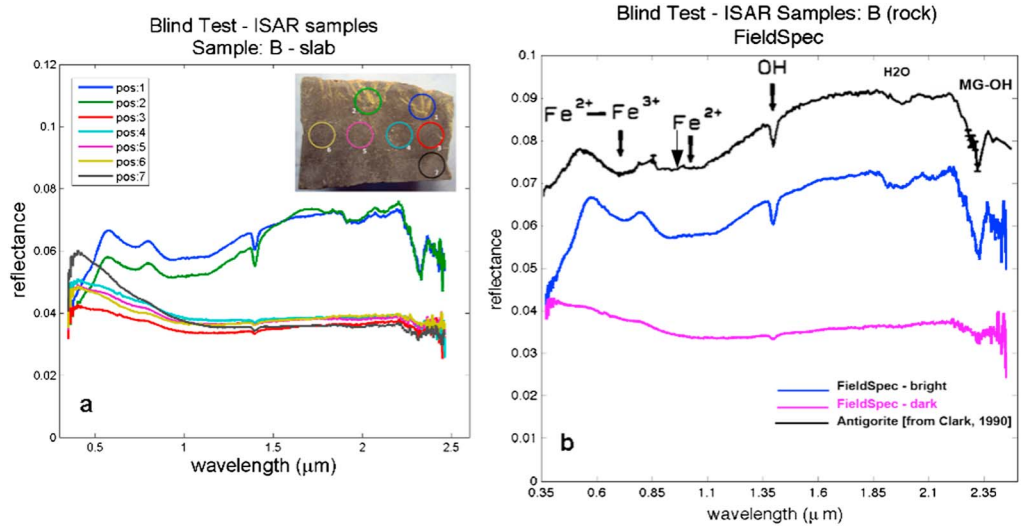

Figure 14. (a) Fieldspec spectra of sample B. The spectra were acquired in different positions on the slab, both in "dark" and in "bright" regions. (b) The typical spectrum of a "dark" region (left, magenta curve) is indicative of dark basaltic glassy material. The typical spectrum of bright/yellowish features on the rock is indicative of serpentine/antigorite (i.e., aqueous alteration of primary mafic materials; blue curve).

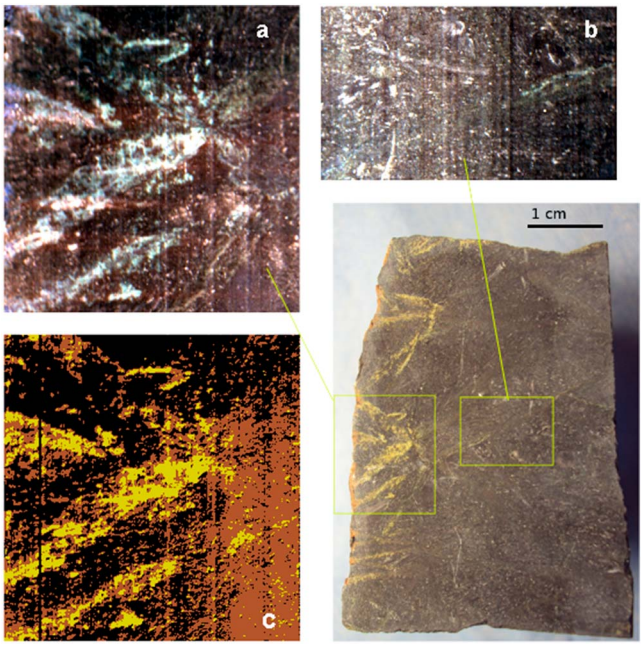

Figure 15. (a) RGB (450; 560; 680 nm) image of the "bright" region; (b) RGB (450; 560; 680 nm) image of the "dark" region. (c) Unsupervised classification of the bright region: the three classes found by isodata algorithm (yellow, brown, and black classes) are each characterized by a different spectrum.

by a blue slope continuum with respect to powders in both the Fieldspec and SPIM. The negative profile of rock slabs is due to optical coupling [*Hapke*, 1993, and references therein], which occurs when particles are so close together that they touch and their surfaces are within approximately a wavelength of each other. Therefore, the relative refractive indices across the grain boundaries are from one mineral to another (whether of different or similar composition), not from the mineral to air or to vacuum. As a result, the overall reflectance from rock slab surfaces is lower and spectrally bluer than in materials with larger grain sizes.

Nervertheless, in the literature, the continuum is described as the combination of different properties of the material that affect a kind of "background" absorption [*Clark*, 1999]. These properties could be due to material texture, grain size, to the relative ratio of instrumental spatial resolution to grain size, occurrence of spectroscopically neutral components, or occurrence of components that show strong absorption in UV range [*Sunshine et al*., 1990]. In particular, a blue slope could be due to a number of factors, including low Fe content in silicates, an amorphous/poorly crystalline nature of the rock, the removal of the finest fraction from larger grain-sized rock, or occurrences of fine-grained magnetite and graphite, and a reduction in silicate absorption band depths [*Cloutis et al*., 2011a, 2011b].

With this in mind, as a general procedure, minerals/rocks characterized by negative slope were identified initially and then the spectral absorption features were interpreted by removing the continuum. The continuum consisted of a first-order polynomial passing between two points at fixed wavelength.

Thus, we infer the "blue slope" affecting the slab spectra to be due to the combination of the effect of optical coupling (slab) and microcrystalline silicate phases, plus opaque grains.

In particular, the profile from sample A matches, in general, that of microcrystalline siliceous rocks, as can be seen from the mean area spectra (Figures 4 and 6).

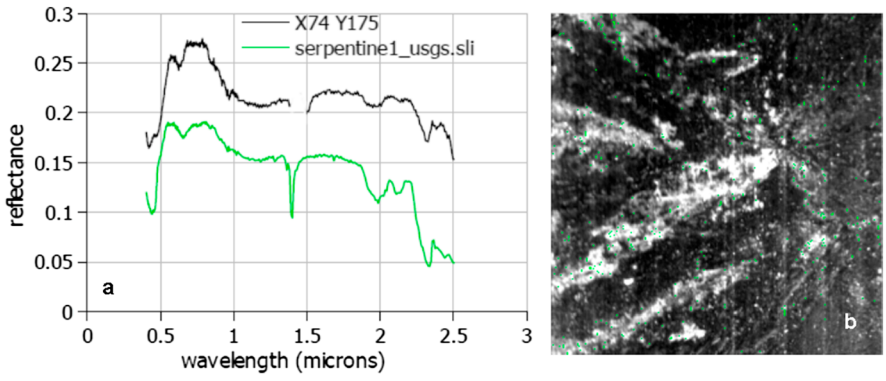

Figure 16. (a) Comparison between the spectral profile of pixel x74 y175 in bright region of sample B and the spectral signature of serpentine 1 from USGS library; (b) mapping of serpentine 1 spectrum on the whole bright area (green pixels).

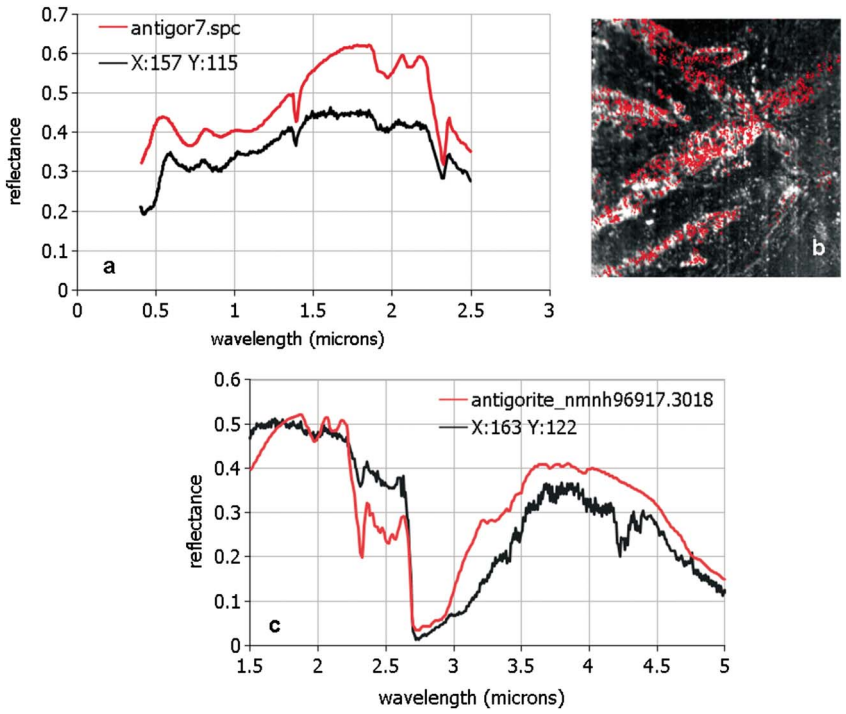

Figure 17. (a) Comparison between the spectral profile of pixel x157 y115 in bright region of sample B and the spectral signature of antigorite 7 from USGS library; (b) mapping of antigorite spectrum on the whole bright area (red pixels); (c) comparison between the spectral profile of pixel x163 y122 in bright region of sample B and the spectral signature of antigorite from RELAB library, in the range between 1.5 and 5 μm.

In sample A, coarser grains in the white layers could be responsible for a more marked blue slope, whereas the occurrence of organic material and/or opaque phases in darker layers could cause the low albedo and a more gentle slope (Figure 5).

In sample B, the low albedo and the negative slope of dark regions is inferred to be a consequence of the presence of glass, mafic minerals, iron oxides, and of the optical coupling (slab).

Removal of the continuum allowed study of the spectral parameters of a single absorption in order to map it on the sample.

The single-pixel spectra of both the samples (see, for example, Figures 6 and 19) show several different absorption features that can be the results of the combination of different phases. In fact, as noted above, the SPIM scan has a spatial resolution of 38 μm, so if the grain size of rock is less than 38 μm, the spectrum

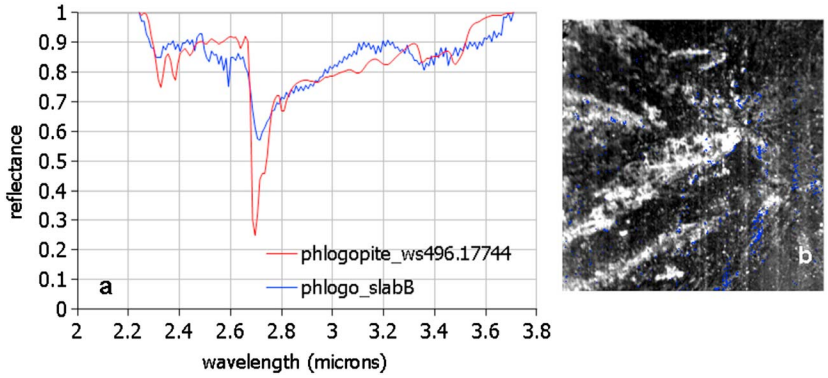

Figure 18. (a) Comparison between the spectral profile of pixel x61y102 in bright region of sample B and the spectral signature of phlogopite from USGS library, range 2.2 and 3.8 μm; (b) mapping of phlogopite on the whole bright area (blue pixels).

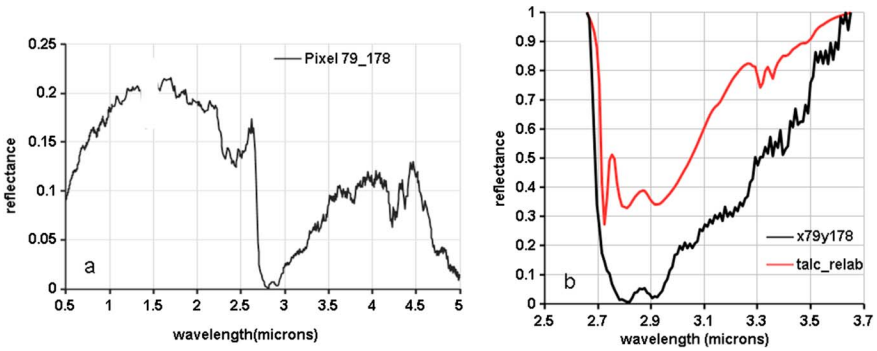

Figure 19. (a) Mg-OH absorption features of the spectral profile of one pixel in bright region of sample B; (b) comparison with the spectral signature of talc from USGS library, range 2.6 and 3.7 μm.

of one pixel will be affected by absorption features corresponding to different grains, minerals, or also to different orientations of the same mineral.

5.2. Interpretation of the Results: Sample A—Fieldspec-SPIM

As shown in Figure 16, the Fieldspec data collected on bright and dark layers allow the identification of the principal absorptions of some mineralogical species occurring in this sample, such as those related to Al-OH bonds, more evident in the powder spectrum.

Sample A is characterized overall by a blue slope that matches that of chert and is, in general, typical of fine-grained rocks. There are some differences between dark and white layers in albedo values that are lower in the dark layers due to smaller grain size and/or organic matter whose occurrence could be observed in some absorption features in the spectral region between 3.2 and 3.5 μm. In particular, in this range the absorptions near 3.3 and 3.4, and 3.48 μm are strictly related to C-H fundamental stretching [*Silverstein et al.*, 1981]. By removing the continuum from some absorption features in the visible region, it was possible to isolate the strong absorption between 0.4 and 0.6 μm in some pixels, (Figures 10 and 11). Strong absorption in this region is compatible with TiO_2, probably in the form of anatase, because of its stability at lower temperature [*Dachille et al.*, 1968]. Moreover, the cooccurrence of absorptions at 0.65 and 0.95 μm could be due to goethite.

Removal of the continuum also allowed identification of phyllosilicate phases in the near infrared region. The phase most readily recognizable is white mica or muscovite/illite, as suggested by the occurrence of absorption features at 2.2 μm followed by 2.35 and 2.45 μm [*Scott*, 1996; *Post and Noble*, 1993]. As reported by *Scott* [1996], it is difficult to distinguish illite K0.65Al2.0[Al0.65Si3.35O10](OH)2 from muscovite KAl2(AlSi3)O10(OH, F)2 by reflectance, although illite appears to exhibit a deeper feature at 1.9 μm [*Scott*, 1996]. In sample A, the band at 1.9 μm is weak or absent; thus, the white mica in sample A is more likely related to muscovite.

The occurrence of microcrystalline quartz (chert), muscovite, and opaques, and the alternation of bright and dark layers are consistent with a sedimentary siliciclastic rock in which the phyllosilicate phases formed by aqueous alteration of minerals of igneous rocks. The precursor rocks could have been acidic because mafic minerals, such as olivine or pyroxene, were not identified (although they could have been completely altered to phyllosilicate). The primary minerals of this sample could have been silica (glass), K-feldspar, and opaques (rutile), which suffered devitrification and aqueous alteration, as summarized in Table 1 and identified by mineralogical techniques [*Bost et al.*, 2013].

5.3. Interpretation of Results: Sample B

The most recognizable mineralogical phase in sample B is antigorite and, in general, the serpentine minerals that occur mainly in the spinifex crystals on the bright region of sample B (see Figure 15a), identified in the data collected by Fieldspec and SPIM. The antigorite is recognizable not only through the band features but also by the shape of the spectrum profile. Data collected by SPIM confirmed the occurrence of antigorite and serpentine group minerals in the SWIR range, in particular, in the shape of the absorption features near 2.75 μm. Around 0.99 μm there is a band that could be related to Fe2+ crystal field (C.F.) absorption, but this

Table 1. Comparison Between Mineralogy of the Samples and Minerals Individuated by SPIM Data

Name of Sample	00 AU05—Sample A	10SA09—Sample B
Mineralogical phases or species, found by optical microscope, IR, Raman, XRD, and Mössbauer (details in *Bost et al*. [2013])	quartz hydromuscovite Ti-oxide	olivine antigorite micas clays hematite magnetite talc
Mineralogical phases or species found by SPIM data	microcrystalline quartz (chert) muscovite Ti-oxide goethite organic matter	antigorite phlogopite (mica) talc

mineral can also indicate the forsteritic olivine found by *Bost et al*. [2013]. Although, the same band could be due to clinopyroxene; for example, Ca-poor augite, and the plagioclase could have decreased the 2 μm absorption band of pyroxene as reported by *Pompilio et al*. [2007]. Neither clinopyroxene nor orthopyroxene was detected by other techniques [*Bost et al*., 2013].

By removing the continuum in the range between 2.2 and 4 μm, other phases were detected, such as phlogopite and talc. This paragenesis implies not only aqueous alteration but also low-grade metamorphic processes compatible with lower greenschist facies.

The occurrences of antigorite and minerals from the serpentine group in a dark rock fragment suggest the possibility of an ultramafic rock in which the probable precursor component was forsteritic olivine and pyroxene. Mg phyllosilicates and amphiboles would be formed by aqueous alteration of olivine and pyroxene. Thus, also in the case of sample B the spectral end-members of SPIM data agree with the composition of the minerals found by *Bost et al*. [2013], (Table 1).

6. Conclusion

This investigation demonstrates the high potential of the SPIM facility. As shown by the results in Table 1, SPIM was able to detect almost all the minerals occurring in the blind test samples. Thanks to the high spatial resolution together with the high spectral resolution, it allows identification of mineralogical species also in fine-grained rocks. In fact, different mineralogical components were identified in the blind test samples after removing the continuum. Moreover, it allowed identification of some absorptions related to organic matter. This aspect is very important in the view of supporting ExoMars 2018 mission, since the first science objective of the ExoMars Rover, is to search for signs of past and present life on Mars.

We have demonstrated that the specific features of SPIM will be very useful for supporting the ExoMars 2018 mission, together with the Ma-MISS and MicrOmega spectrometers, as well as VIR-MS/VIRTIS-like spectrometer's data on board the Dawn and other planetary missions. Thus, this facility will improve the inversion models and help to better explain the spectral data collected by "spot" spectrometers on rocks and "on ground."

Furthermore, SPIM could be very useful as a noninvasive diagnostic research method facility for analyzing minute quantities or particle sizes of different meteorite groups, as well as samples returned from future space missions.

Acknowledgments
The authors thank the Italian Space Agency (ASI) through grant I/004/12/0. Spectral new data to this paper could be requested from Maria Cristina De Sanctis mariacristina.desanctis@iaps.inaf.it; data on mineralogical and technical characterization of the samples are properly cited and referred to in the reference list.

References

Bost, N. (2012), *Geochemical and Mineralogical Analysis of Mars Analogue Materials and the Creation of the International Space Analogue Rock Store (ISAR). Geochemistry*, Universite d'Orleans.

Bost, N., F. Westall, C. Ramboz, F. Foucher, D. Pullan, A. Meunier, S. Petit, I. Fleischer, G. Klingelhöfer, and J. L. Vago (2011), 2018 MAX-C/ExoMars mission: The Orleans Mars-analogue rock collection for instrument testing, 42nd Lunar and Planetary Science Conference, Abstract #1347

Bost, N., F. Westall, F. Gaillard, C. Ramboz, and F. Foucher (2012), Synthesis of a spinifex-textured basalt as an analog to Gusev crater basalts, Mars, *Meteorit. Planet. Sci.*, *47*(5), 820–831.

Bost, N., F. Westall, C. Ramboz, F. Foucher, D. Pullan, A. Meunier, S. Petit, I. Fleischer, G. Klingelhöfer, and J. L. Vago (2013), Missions to Mars: Characterization of Mars analogue rocks for the International Space Analogue Rockstore (ISAR), *Planet. Space Sci.*, *82–83*, 113–127.

Bost, N., et al. (2015), Testing the ability of the ExoMars 2018 payload to document geological context and potential habitability on Mars, *Planet. Space Sci.*, *108*, 87–97.
Clark, R. N. (1999), Chapter 1: Spectroscopy of rocks and minerals, and principles of spectroscopy, in *Manual of Remote Sensing, Volume 3*, *Remote Sensing for the Earth Sciences*, edited by A. N. Rencz, John Wiley, New York.
Cloutis, E. A., T. Hiroi, M. J. Gaffey, C. M. O. D. Alexander, and P. Mann (2011a), Spectral reflectance properties of carbonaceous chondrites: 1. CI chondrites, *Icarus*, *212*(1), 180–209.
Cloutis, E. A., P. Hudon, T. Hiroi, M. J. Gaffey, and P. Mann (2011b), Spectral reflectance properties of carbonaceous chondrites: 2. CM chondrites, *Icarus*, *216*(1), 309–346.
Coradini, A., et al. (2001), Ma_Miss: Mars multispectral imager for subsurface studies, *Adv. Space Res.*, *28*(8), 1203–1208.
Coradini, A., et al. (2011), Laboratory measurements in support of the DAWN mission: The SPectral IMaging (SPIM) facility, EPSC abstracts, vol. 6, 1043.
Dachille, F., P. Y. Simons, and R. Roy (1968), Pressure-temperature studies of anatase, brookite, rutile and TiO2 + II, *Am. Mineral.*, *53*, 1929.
De Angelis, S., M. C. De Sanctis, E. Ammannito, C. Carli, T. Di Iorio, and F. Altieri (2014), The Ma_Miss instrument performance, I: Analysis of rocks powders by Martian VNIR spectrometer, *Planet. Space Sci.*, *101*, 89–107.
De Angelis, S., et al. (2015), The spectral imaging facility: Setup characterization, *Rev. Sci. Instrum.*, *86*(9), 1–15.
De Sanctis, M. C., et al. (2010), The VIR spectrometer, *Space Sci. Rev.*, *163*(1–4), 329–369.
de Vries, S. T. (2004), Early Archaean sedimentary basins: depositional environment and hydrothermal systems, *Geol. Ultraiectina*, *244*, 1–160.
de Vries, S. T., W. Nijman, J. R. Wijbrans, and D. R. Nelson (2006), Stratigraphic continuity and early deformation of the central part of the Coppin Gap Greenstone Belt, Pilbara, Western Australia, *Precambrian Res.*, *147*, 1–27.
Gaffey, S. (1985), Reflectance spectroscopy in the visible and near-infrared (0.35–2.55 μm): applications in carbonate petrology, *Geology*, *13*, 270–273.
Gaffey, S. (1986), Spectral reflectance of-carbonate minerals in the visible and near infrared (0.35–2.55 μm): calcite, aragonite, and dolomite, *Am. Mineral.*, *71*, 151–162.
Hapke, B. (1993), *Theory of Reflectance and Emittance Spectroscopy*, Cambridge Univ. Press, Cambridge, U. K.
Mangold, N., et al. (2009), Mineralogy of recent volcanic plains in the Tharsis region, Mars, and implications for platyridged flow composition, *Earth Planet. Sci. Lett.*, *294*, 440–450, doi:10.1016/j.epsl.2009.07.36.
Nna-Mvondo, D., and J. Martinez-Frias (2007), Komatiites: From Earth's geological settings to planetary and astrobiological contexts, *Earth Moon Planets*, *100*, 157–179.
Orberger, B., V. Rouchon, F. Westall, S. T. de Vries, D. L. Pinti, C. Wagner, R. Wirth, and K. Hashizume (2006), Microfacies and origin of some Archean cherts (Pilbara, Australia), *Geol. Soc. Am.*, *405*, 133–156.
Pompilio L., M. Sgavetti, and G. Pedrazzi (2007), Visible and near-infrared reflectance spectroscopy of pyroxene-bearing rocks: New constraints for understanding planetary surface compositions, *J. Geophys. Res.*, *112*, E01004, doi:10.1029/2006JE002737.
Post, J. L., and P. N. Noble (1993), The near infrared combination band frequencies of dioctahedral smectites, micas, and illites, *Clays Clay Miner.*, *41*, 639–644.
Scott, K. (1996), Composition of white mica in weathered rocks: Indicator of rock type and proximity of gold mineralization, Western Australia, *Explore*, *93*, 3–5.
Silverstein, R. M., G. C. Bassler, and T. C. Morrill (1981), *Spectrometric Identification of Organic Compounds*, 4th ed., John Wiley and Sons, New York.
Sunshine, J. M., C. M. Pieters, and S. F. Pratt (1990), Deconvolution of mineral absorption bands: An improved approach, *J. Geophys. Res.*, *95*, 6955–6966, doi:10.1029/JB095iB05p06955.
Vago, J., et al. (2013), ExoMars: ESA's next step in Mars Exploration, *Bull. Eur. Space Agency*, *155*, 12–23.
Westall F., et al. (2006), The 3.466 Ga "Kitty's Gap Chert", an Early Archean microbial ecosystem, *Geol. Soc. Am.*, *405*, 105–131 (special paper).
Westall, F., and B. Cavalazzi (2011), Biosignatures in rocks, in *Encyclopedia of Geobiology*, edited by V. Thiel and J. Reitner, pp. 189–201, Springer, Berlin.